Ag$_3$PO$_4$ decorated black urchin-like defective TiO$_2$ for rapid and long-term bacteria-killing under visible light

Yingde Xu [a], Xiangmei Liu [b],*, Yufeng Zheng [c], Changyi Li [d], Kelvin Wai Kwok Yeung [e], Zhenduo Cui [a], Yanqin Liang [a], Zhaoyang Li [a], Shengli Zhu [a], Shuilin Wu [a],**

[a] School of Materials Science & Engineering, The Key Laboratory of Advanced Ceramics and Machining Technology By the Ministry of Education of China, Tianjin University, Tianjin, 300072, China
[b] Hubei Key Laboratory of Polymer Materials, Ministry-of-Education Key Laboratory for the Green Preparation and Application of Functional Materials, School of Materials Science & Engineering, Hubei University, Wuhan, 430062, China
[c] College of Engineering, State Key Laboratory for Turbulence and Complex System, Department of Materials Science and Engineering, Peking University, Beijing, 100871, China
[d] Stomatological Hospital, Tianjin Medical University, Tianjin, 300070, China
[e] Department of Orthopaedics & Traumatology, Li Ka Shing Faculty of Medicine, The University of Hong Kong, Pokfulam, Hong Kong, 999077, China

ARTICLE INFO

ABSTRACT

Both phototherapy via photocatalysts and physical puncture by artificial nanostructures are promising substitutes for antibiotics when treating drug-resistant bacterial infectious diseases. However, the photodynamic therapeutic efficacy of photocatalysts is seriously restricted by the rapid recombination of photogenerated electron–hole pairs. Meanwhile, the nanostructures of physical puncture are limited to two-dimensional (2D) platforms, and they cannot be fully used yet. Thus, this research developed a synergistic system of Ag$_3$PO$_4$ nanoparticles (NPs), decorated with black urchin-like defective TiO$_2$ (BU–TiO$_{2\text{-X}}$/Ag$_3$PO$_4$). These NPs had a decreased bandgap compared to BU-TiO$_{2\text{-X}}$, and BU-TiO$_{2\text{-X}}$/Ag$_3$PO$_4$ (3:1) exhibited the lowest bandgap and the highest separation efficiency for photogenerated electron–hole pairs. After combination with BU-TiO$_{2\text{-X}}$, the photostability of Ag$_3$PO$_4$ improved because the oxygen vacancy of BU-TiO$_{2\text{-X}}$ retards the reduction of Ag$^+$ in Ag$_3$PO$_4$ into Ag^0, thus reducing its toxicity. In addition, the nanospikes on the surface of BU-TiO$_{2\text{-X}}$ can, from all directions, physically puncture bacterial cells, thus assisting the hybrid's photodynamic therapeutic effects, alongside the small amount of Ag$^+$ released from Ag$_3$PO$_4$. This achieves synergy, endowing the hybrid with high antibacterial efficacy of 99.76 ± 0.15% and 99.85 ± 0.09% against *Escherichia coli* and *Staphylococcus aureus*, respectively, after light irradiation for 20 min followed by darkness for 12 h. It is anticipated that these findings may bring new insight for developing synergistic treatment strategies against bacterial infectious diseases or pathogenic bacterial polluted environments.

1. Introduction

By 2050, the long-term overuse of antibiotics may lead to a tenfold increase in the rate of mortality from incurable infections [1]. Since bacteria have become resistant to antibiotics, new antibacterial materials and techniques are emerging with increasing speed. It takes only two weeks for bacteria to develop resistance to new antibiotics that have taken several years, and great expense, to be developed [2–4]. Accordingly, innovative, antibiotics-free treatment strategies are expected; bacteria would either have no drug resistance to these treatments or could not develop resistance in a short time. Among new therapeutic methods [5–9], photodynamic therapy (PDT) can effectively inactivate bacteria via the reactive oxygen species (ROS) quickly produced by certain photo-responsive materials under light irradiation. Titanium dioxide (TiO$_2$) is one of most common semiconductor photocatalysts, but its large bandgap of 3.0–3.2 eV restricts its phototherapy application because it can only be excited by ultraviolet (UV) light [10,11]. Although black TiO$_2$, due to the lower bandgap and large amount of oxygen vacancy on its surface [12,13], exhibits better photocatalytic performance than untreated TiO$_2$, the fatal flaw of using a

mono-photocatalyst for phototherapy is the rapid recombination of electron–hole pairs [14,15], which reduce ROS yields under light irradiation. A heterojunction composed of two or more semiconductors could benefit the transfer of photo-generated electrons between different components, thus relieving this issue to some extent [16–18].

Trisilver phosphate (Ag_3PO_4), an important semiconductor with an indirect bandgap (2.36 eV), is attracting the increasing attention in the photocatalytic field because of its great oxidation capacity [19]. However, the reduction power of Ag_3PO_4 under visible light irradiation is too weak to conduct a photocatalytic reaction, which causes serious photo-corrosion of the Ag_3PO_4 [20,21]. However, a sacrificial reagent, such as silver nitrate ($AgNO_3$) can suppress the Ag^+ of Ag_3PO_4 to form Ag^0, which is conducive to the photostability of Ag_3PO_4 [22,23]. However, it is unrealistic to provide a sacrificial agent for Ag_3PO_4 in biologic applications. The Ag_3PO_4 particle also maintains a relatively large size (0.5–2 μm), which further affects its photocatalytic efficiency because it has a low specific surface area [22]. Loading Ag_3PO_4 on other semiconductors or two-dimensional (2D) materials can effectively enhance its photostability of and reduce its size [24–26], whereas Ag_3PO_4-based traditional heterojunction and Z-scheme heterojunction either weaken its oxidation/reduction capacity or decrease the number of photoexcited carriers, which also weakens the photocatalytic performance [27–35].

Recent studies have disclosed that single-mode treatment cannot achieve ideal therapeutic effects for bacterial infectious diseases [36]. Higher concentrations of ROS are essential for effective photodynamic bacteria-killing [37,38], but large amounts of ROS are harmful for normal tissues [7,36]. In addition, both the lifespan and action radius of ROS are very finite [39,40], making them effective only for killing bacteria with which they come into direct contact. A higher photothermal temperature is necessary for inactivating bacteria effectively during photothermal therapy, but such a temperature will inevitably damage normal cells and tissues [6,41]. Therefore, synergistic action through two or more therapeutic modes has been proven to be more effective for killing bacteria—such as photodynamic therapy paired with Ag ions [42,43] or with photothermal action [44–47], as well as combined photodynamic and photothermal therapy paired with Zn^{2+} [48], Cu^{2+} [49], etc.

Physical puncture has also been reported to be an effective bacteria-killing mode, which neither produces bacterial resistance nor damages normal tissues and cells [50–52]. A few studies have been carried out to determine whether nanospikes or nanorods on a planar substrate could puncture the bacterial cell envelope [50,53,54]. However, these 2D approaches are not suitable for solution-based three-dimensional (3D) environment. As far as the current authors know, no reports have considered the synergy of phototherapy and mechanical puncture

without a planar substrate. Therefore, since TiO_2 has various morphologies, including one-dimensional (1D) nanotubes [55], nanorods [56], 2D nanosheets [57], and 3D nanoflowers [58], in addition to its aforementioned outstanding photocatalytic performance, the authors hypothesized that photodynamic therapy and physical puncture may be combined to achieve satisfactory synergistic efficacy without adverse effects.

Based on this hypothesis, the researchers constructed a heterojunction system, in which Ag_3PO_4 nanoparticles (NPs) were grown *in situ* on black, urchin-like TiO_{2-X}. This created NPs have large amount of surface oxygen defects (BU–TiO_{2-X}). The synthesis process of BU-TiO_{2-X}/Ag_3PO_4 is schematically illustrated in Scheme 1. Surface deficiencies such as oxygen vacancy on the surface of urchin-like TiO_2 produced by $NaBH_4$, can serve as the nucleation site of Ag_3PO_4, and a large number of nanospikes on the surface of black urchin-like TiO_{2-X} restricted the growth of Ag_3PO_4, leading to a higher specific surface area than pure and unloaded Ag_3PO_4 [15,58,59]. Therefore, black urchin-like TiO_{2-X}/Ag_3PO_4 NPs, under visible light, can inactivate bacteria in a short period of time. In addition, the extensive nanospikes of the black urchin-like TiO_{2-X} NPs, combined with the Ag^+ released by Ag_3PO_4 in water, inhibit bacterial growth in long term [25].

2. Experimental

2.1. Materials

Anhydrous ethanol, silver nitrate ($AgNO_3$), disodium hydrogen phosphate (Na_2HPO_4), hydrogen peroxide (H_2O_2, 30%) and sodium boron hydride ($NaBH_4$, 98%) were all purchased from Aladdin (Shanghai). Nitric acid (HNO_3, 65.0%–69.0%) and sodium hydroxide (NaOH, 96%) were purchased from Jiangtian (Tianjin). TiO_2 (Macklin P25) was purchased from Macklin (Shanghai).

2.2. Urchin-like TiO_2 NPs fabrication

Urchin-like TiO_2 NPs were synthesized via a two-stage hydrothermal reaction with slight modifications [58]. Briefly, TiO_2 (Macklin P25) powders (1 g) were dispersed in 60 mL of a NaOH aqueous solution (5 M), continuously stirred for 30 min, and then transferred into a Teflon-lined, stainless-steel autoclave and heated at 120 °C for 24 h. After reaction, the precipitates were collected by centrifugation, and subsequently washed with deionized (DI) water five times. These precipitates were dried at 60 °C in a vacuum for further use. The dried precipitates (0.3 g) were dispersed in a mixture of 57 mL of the NaOH aqueous solution (1 M) and 3 mL of a H_2O_2 (30%) solution. The
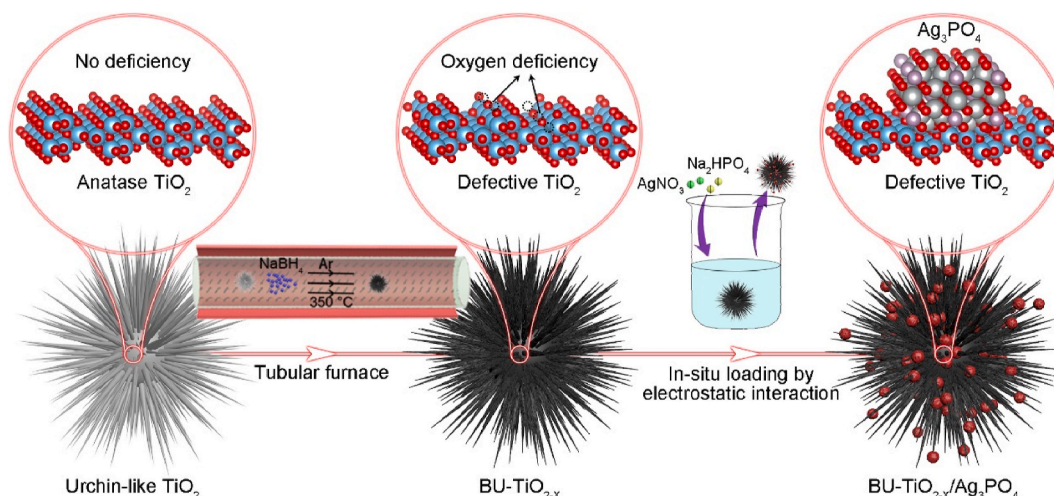
Scheme 1. The synthesis process of BU-TiO_{2-X}/Ag_3PO_4.

suspension was stirred magnetically, ultrasonicated for 30 min, and then transferred into a Teflon-lined, stainless-steel autoclave at 150 °C for 8 h. The precipitates were again collected by centrifugation, washed with DI water five times, and dried at 60 °C in a vacuum to generate urchin-like sodium titanate particles. The urchin-like particles were then treated with excess HNO$_3$ solution (0.1 M) with continuous magnetic stirring to produce urchin-like hydrogen titanate particles. The urchin-like hydrogen titanate particles were then washed with DI water five times and calcined at 400 °C for 1 h to produce the urchin-like TiO$_2$ particles.

2.3. Black urchin-like TiO$_{2-X}$ NP fabrication

0.5 g of urchin-like TiO$_2$ powders were mixed with 0.5 g of NaBH$_4$, and the mixture was thoroughly ground for 30 min under the infrared baking lamp [60,61]. The mixture then was placed in a tubular furnace and heated at a rate of 5 °C min^{-1} to 350 °C, and then kept for 2 h under an argon atmosphere with subsequent furnace cooling to room temperature. The collected powders were rinsed with ethanol and DI water repeatedly.

2.4. Black urchin-like TiO$_{2-X}$/Ag$_3$PO$_4$ NPs fabrication

The black urchin-like TiO$_{2-X}$/Ag$_3$PO$_4$ NPs were synthesized via the following process. Briefly, 0.4 g of synthesized black urchin-like TiO$_{2-X}$ powders were added to 100 mL of ethanol under ultrasonication. A stoichiometric amount of AgNO$_3$ was mixed with the black urchin-like TiO$_{2-X}$ suspension and vigorous stirred for 1 h. During the stirring process, stoichiometric Na$_2$HPO$_4$ dissolved in 20 mL of distilled water, was added, drop by drop, into the above dispersion. The mixture was then continuously stirred for 3 h. The obtained precipitates were separated by centrifugation and washed eight times with ethanol and DI water. The prepared powders were then dried overnight in a vacuum oven at 60 °C. The entire synthesis was carried out in the dark. Pure and unloaded Ag$_3$PO$_4$ was prepared under identical experimental conditions without the presence of black urchin-like TiO$_{2-X}$.

2.5. Characterizations

The crystal structures of TiO$_2$ NPs and Ag$_3$PO$_4$ were determined using an X-ray diffractometer (XRD; D8 Advanced, Germany) with Cu-Kα as the radiation source (λ = 1.5406 Å). Samples and bacteria morphologies were observed via scanning electron microscope (SEM; Hitachi S-4800, Japan) analysis equipped with an energy-dispersive X-ray spectroscopy (EDS; Oxford X-max20, UK) and a transmission electron microscopy (TEM; JEM-2100F, Japan). The elements composition of the samples were measured via X-ray photoelectron spectroscopy (XPS; Escalab250Xi, Thermofisher, USA), and Raman spectra were conducted by using a Thermo-scientific DXR spectrometer in the range of 100–1000 cm^{-1}.The ultraviolet–visible (UV–Vis) diffuse reflectance (DRS) optical properties of the samples were measured via the Japanese Shimadzu UV-2700 spectrophotometer, with the measurement range set to 200–800 nm and using barium sulfate (BaSO$_4$) as a reference. The steady state photoluminescence (PL) of the samples was examined via a fluorolog-3 fluorescence spectrophotometer (HORIBA), with an excitation wavelength of 365 nm, to illustrate the separation and recombination efficiency of photogenerated electron–hole pairs on irradiated nano-semiconductors. The photocatalytic properties of the samples were investigated via electron spin resonance (ESR; JES-FA200) spectroscopy to detect the ROS by a capture agent (5,5-Dimethyl-1-pyrroline N-oxide).

2.6. Photo-electrochemical performance

Transient photocurrent response measurement and linear sweep voltammetry (LSV) were carried out to further illustrate the photocatalytic performance of the samples under visible light irradiation. Samples were tested on an electrochemical workstation (Gamry Instrument, INTERFACE 1000) in a standard three-electrode system, and the electrolyte was a 0.5 mol L^{-1} sodium sulfate (Na$_2$SO$_4$) aqueous solution. The photocatalyst samples were created as follows: 8 mg of the samples and 80 μL Nafion were added to 2 mL of ethanol to create a solution under ultrasonication. Then 80 μL of the mixed solution were added to a 10 × 10 mm indium tin oxide (ITO) glass electrode to make a coating.

2.7. Ag ions release

Ag$_3$PO$_4$ and BU-TiO$_{2-X}$/Ag$_3$PO$_4$ samples soaked in 100 mL of DI water (pH = 7.4), were stored in darkness at 37 °C for 21 days. 3 mL of the solutions were sucked out by a pipette gun at 1, 2, 3, 5, 7, 10, 14, and 21 days and added another 3 mL of DI water as supplementary. Ag$^+$ released concentration was detected via inductively coupled plasma-optical emission spectrometry (ICP-OES; ICAP7000 series).

2.8. In vitro antimicrobial tests

The samples' antimicrobial performances were tested against typical bacteria—*Staphylococcus aureus* (*S. aureus*) and *Escherichia coli* (*E. coli*)—through the spread plate method. The bacterial suspension was cultured separately in sterile Luria−Bertain (LB) media at 37 °C and was then diluted with LB media to 10^7 CFUmL^{-1} before use. After being mixed with 200 μL of diluted bacterial suspension, all samples (control, BU-TiO$_{2-X}$, Ag$_3$PO$_4$, BU-TiO$_{2-X}$/Ag$_3$PO$_4$ (6:1), BU-TiO$_{2-X}$/Ag$_3$PO$_4$ (3:1), BU-TiO$_{2-X}$/Ag$_3$PO$_4$ (1:1)), at concentrations of 200 ppm, were added to 96-well plates. Each sample was irradiated with double solar intensity for 20 min via the Xenon lamplight to simulate natural light. All samples have matched to samples without irradiation. Moreover, the samples, including the control, BU-TiO$_{2-X}$, Ag$_3$PO$_4$, BU-TiO$_{2-X}$/Ag$_3$PO$_4$ (3:1) and BU-TiO$_{2-X}$/Ag$_3$PO$_4$ (3:1) +light (20 min), were mixed with the bacterial suspension and placed in a constant-temperature shaker set to 160 rpm at 37 °C for 12 h without irradiation. In the end, each 20 μL amount of diluted solution was spread, in a well-distributed fashion, on the agar plate, which was then cultured at 37 °C for 24 h. The antibacterial rate of each plate was calculated by measuring the number of bacterial colonies on the plate according to the following equation:

Antibacterial ratio (%) = (number of CFUs in control sample - number of CFUs in experimental sample) / (number of CFUs in control sample) × 100%   (1)

The bacterial morphology changes were observed via SEM. After being treated with the above procedures, the 96-well plate was deposited for 2 h. Then, the bacteria were fixed for 2 h with 200 μL of 2.5% glutaraldehyde in the dark. Subsequently, handled with 30%, 50%, 70%, 90%, and 100% ethanol solutions were applied to dehydrate bacteria, with each step taking 15 min. The bacterial morphology was observed by SEM after drying.

2.9. Simulation computation methods of cell membrane puncture

Cell membrane penetration was conducted in a Finite Element Modeling (FEM) environment (COMSOL Multiphysics), and the process of a bacterium being punctured was simulated by the model of an inflated shell with isotropic elasticity being punctured by a nanospike. The researchers hypothesized that Young's modulus (E) would encompass the entire cell envelope in these simulations and that the modulus of *S. aureus* and *E. coli* should be 30 MPa and 5 MPa, respectively [53,62]. The bacterial turgor pressure (ΔP) can be assessed by the modulus of *S. aureus* and *E. coli*, and the ratio of the turgor pressure to the modulus can be considered a constant (E/ΔP~100) [63]. The *E. coli* model was assumed to have a spherocylindrical shape, with a radius of 250 nm and a length of 2000 nm, while *S. aureus* model was assumed to have a

spherical shape, with a radius of 250 nm, according to the statistical data from the SEM results. The researchers hypothesized that the driving force for bacterial deformation would be the centripetal force of BU-TiO$_{2-X}$ and could be written as:

$$F_c = M_{BU}\omega^2 R, \tag{2}$$

where M_{BU} is the mass of BU-TiO$_{2-X}$; ω is the angular velocity; and R is the mean moving radius of BU-TiO$_{2-X}$ in the constant-temperature shaker. Based on the above conditions, the driving force could be calculated and was approximately 150 pN. In addition, both *E. coli* and *S. aureus* were punctured by a truncated cone nanospike, the mean diameter was 20 nm.

2.10. In vitro cell viability

Cell cytotoxicity was assessed via the water-soluble tetrazole (2-(2-methoxy-4nitrobenzene)-3-(4-nitrobenzene) -5- (2,4-disulfobenzene) -2H-tetrazole monosodium salt) (CCK-8) method using NIH-3T3 cells. All samples and 96-well plates were disinfected with UV light for 30 min. During the cytotoxicity assay, the samples were dipped in the cell culture medium for one, three, and five days, and the leach liquors (cell density 1×10^5 cellsmL^{-1}) were placed in the 96-well plate and cultured for one, three, and five days in a 5% carbon dioxide (CO$_2$) incubator at 37 °C. Then, 10 μL of the CCK-8 solution were added to the cell culture medium and put in the CO$_2$ incubator for 2.5 h. Finally, the cell viability

of each sample was measured through a microplate reader (wavelengths of 450 nm), which can obtain the optical density (OD).

2.11. Statistical analysis

All the quantitative data were analyzed by the one-way ANOVA and expressed as means ± standard deviations with n = 3. P values < 0.05 were considered statistically significant.

3. Results and discussion

3.1. Morphologies and structure

Fig. 1 shows the morphologies of prepared BU-TiO$_{2-X}$ and BU-TiO$_{2-X}$/Ag$_3$PO$_4$ with different molar ratios of BU-TiO$_{2-X}$ and Ag$_3$PO$_4$ (6:1, 3:1, 1:1). The synthesized BU-TiO$_{2-X}$ particle clearly exhibited an urchin-like structure (Fig. 1(a)) composed of numerous nanospikes (Fig. 1(b)). After *in situ* growth of Ag$_3$PO$_4$, small nanoparticles appeared uniformly on the surfaces of the nanospikes (marked by red arrows in Fig. 1(c), (d), and (e)), and, as the Ag$^+$ content increased during the *in situ* loading process, the number of Ag$_3$PO$_4$ nanoparticles also increased, as proven by the corresponding EDS, shown in Fig. 1(f), (g), and (h). The average size of these nanoparticles was about 10 nm. In contrast, the synthesized Ag$_3$PO$_4$ exhibited a far larger size of over 200 nm under the same conditions but without BU-TiO$_{2-X}$ (Fig. S1), indicating that the BU-TiO$_{2-X}$
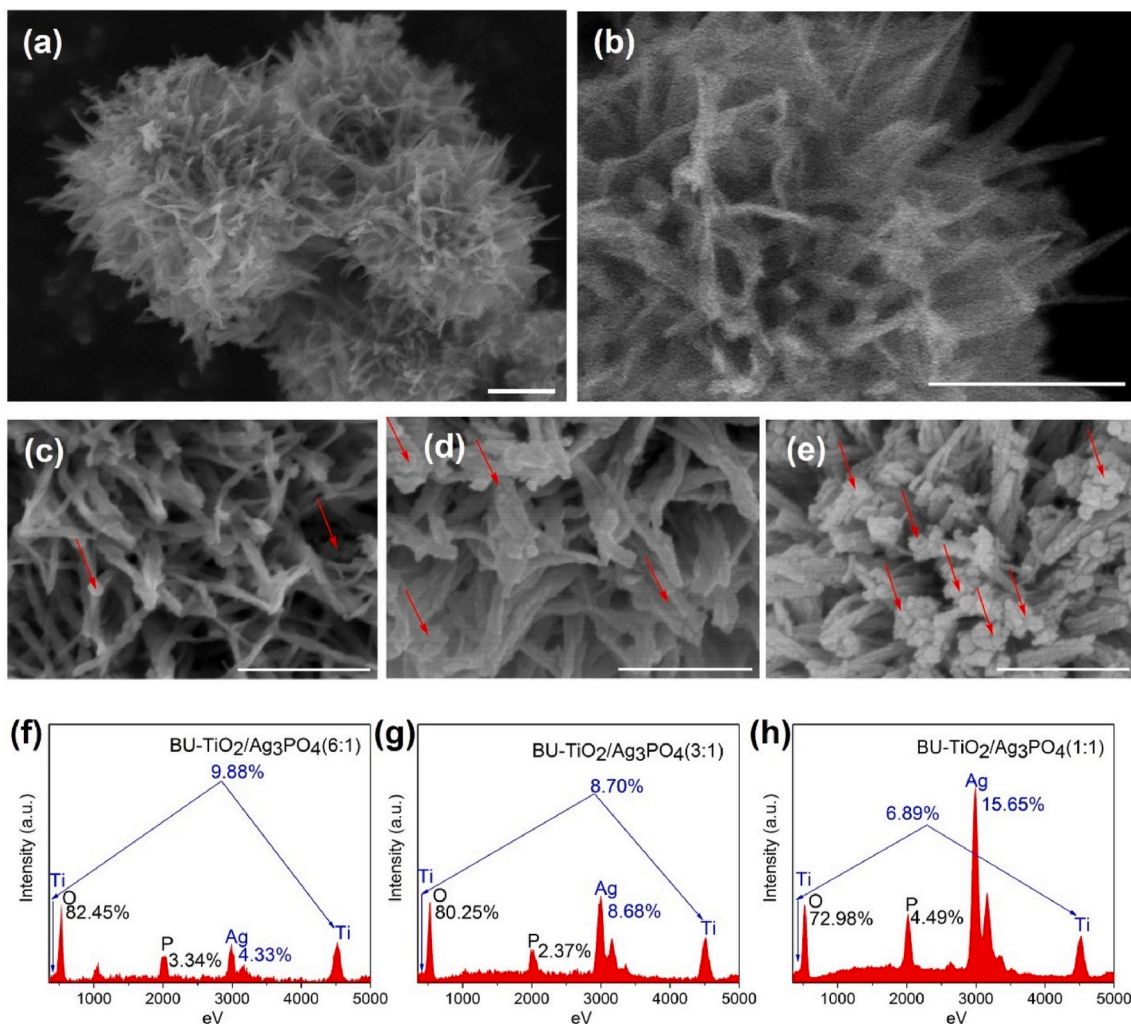

Fig. 1. Morphologies and elements of synthesized materials: (a) FE-SEM image of BU-TiO$_{2-X}$; (b) high magnification image of A; (c), (d), (e) FE-SEM images and (f), (g), (h) Energy dispersive spectroscopy of BU-TiO$_{2-X}$, BU-TiO$_{2-X}$/Ag$_3$PO$_4$ (6:1, 3:1, 1:1). (Scale bar: 300 nm).

nanospikes provided many nucleation sites for Ag_3PO_4 and facilitated the distribution of Ag_3PO_4 on BU-TiO_{2-X}.

The TEM patterns of U–TiO_2, BU-TiO_{2-X}, and BU-TiO_{2-X}/Ag_3PO_4 are shown in Fig. 2(b). The Ag_3PO_4 nanoparticles were successfully loading on the surface of nanospikes, which is in accordance with the SEM results. The areas marked by white, dashed circles represent high-resolution TEM (HRTEM) images of U–TiO_2, and they reveal that the lattice spacings of 0.354 nm and 0.190 nm corresponded to the anatase (101) plane and (200) plane, respectively [64] (Fig. 2(b)). The HRTEM image of BU-TiO_{2-X} showed that the lattice spacing of 0.354 nm corresponded to the anatase (101) plane, while the HRTEM image of BU-TiO_{2-X}/Ag_3PO_4 showed that lattice spacings of 0.190 nm and 0.245 nm corresponded to the anatase (200) plane and the Ag_3PO_4 (211) plane [64]. Some clearly observable oxygen defects and disorders are outlined by the yellow circles. The introduction of surface oxygen defects and disorders restrained the recombination of photogenerated electron–hole pairs via carrier trapping.

The XRD patterns in Fig. 2(c) show the crystal structure and phase composition of the as-synthesized U–TiO_2, BU-TiO_{2-X}, Ag_3PO_4, and BU-TiO_{2-X}/Ag_3PO_4 (6:1, 3:1, 1:1) samples. In the XRD pattern for U–TiO_2, the characteristic peaks at 2θ values of 25.3°, 37.7°, 48.0°, and 53.8° corresponded to the (101), (004), (200), and (211) crystal planes of the anatase phase [65], indicating that U–TiO_2 was successfully formed

during the hydrothermal reaction. After U–TiO_2 received a reduction treatment in a tubular furnace at 350 °C (Scheme 1), the corresponding peaks became weak and their breadth decreased, indicating that an oxygen-deficient amorphous TiO_{2-X} layer generated, which is in line with the HRTEM results in Fig. 2(b). In the case of the synthesized Ag_3PO_4 sample, the XRD pattern contained diffraction peaks at 2θ values of 20.8°, 29.7°, 33.3°, 36.6°, 47.8°, 52.7°, 55.0°, 57.2°, and 71.9°, which were assigned to the (110), (200), (210), (211), (310), (222), (320), (321), and (332) crystal planes of Ag_3PO_4 [19], suggesting that Ag_3PO_4 was successfully prepared. Meanwhile, the XRD patterns of BU-TiO_{2-X}/Ag_3PO_4 (6:1, 3:1, 1:1) showed that the peaks intensity was successively increased, indicating that the Ag_3PO_4 content had also increased in the hybrid. Under visible light for 20 min after three circles, the Ag_3PO_4 of XRD pattern presented the Ag peaks, while BU-TiO_{2-X}/Ag_3PO_4 (3:1) still contained no Ag peaks in Fig. S2, indicating that the oxygen vacancy on the surface of BU-TiO_{2-X} can retard the photo-corrosion of Ag_3PO_4 [66]. To further verify the crystalline structure of the as-synthesized U–TiO_2 and BU-TiO_{2-X}, Raman spectroscopy was conducted (Fig. 2(d)). The Raman vibration peaks of the U–TiO_2, centered at around 143, 197, 394, 515, and 637.0 cm^{-1}, were well ascribed to the E_g, E_g, B_{1g}, $A_{1g} + B_{1g}$, and E_g characteristic vibration modes of anatase [67]. In the inset of Fig. 3(d), a positive shift in BU-TiO_{2-X} can be observed, indicating that oxygen defects (such as
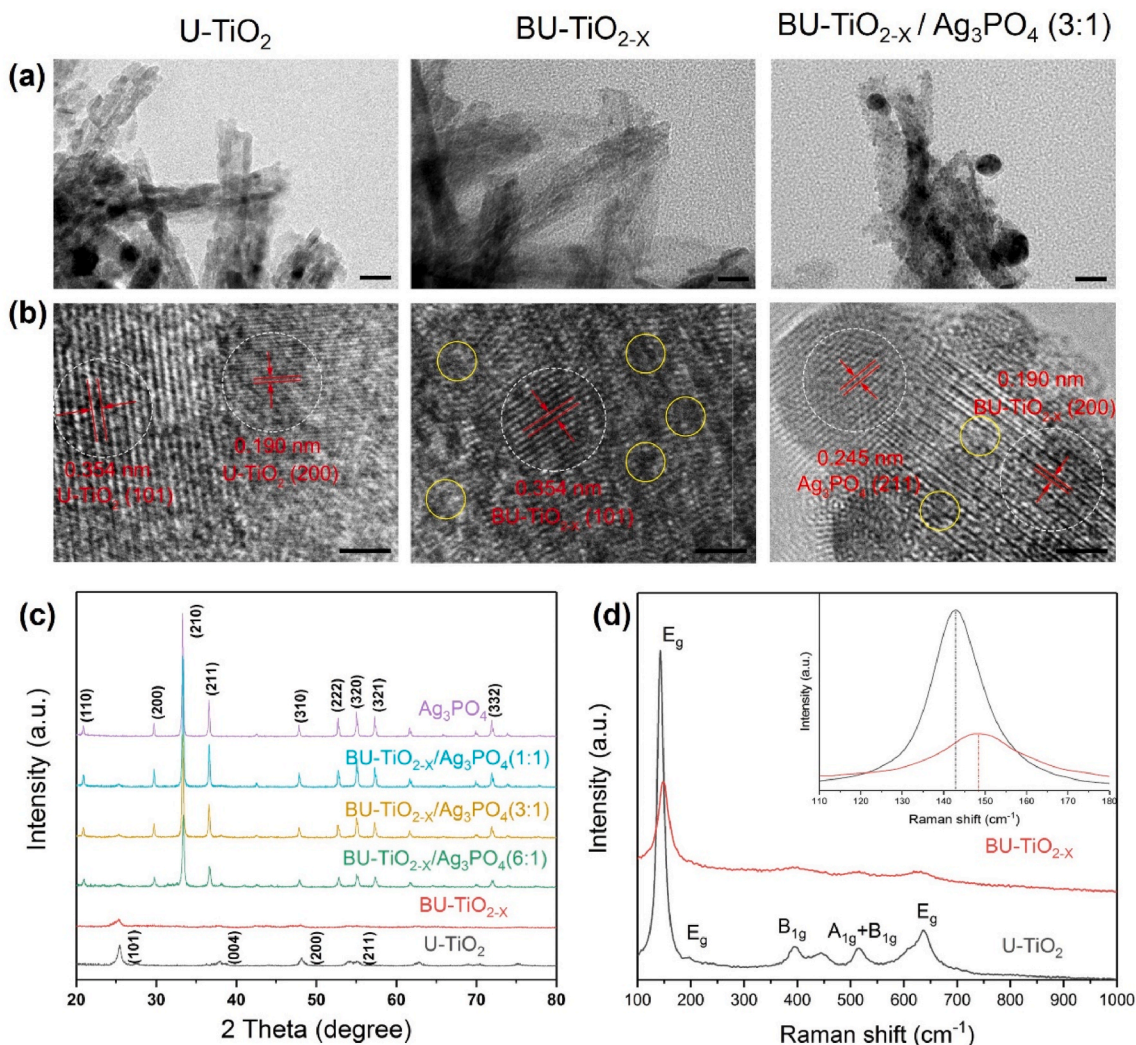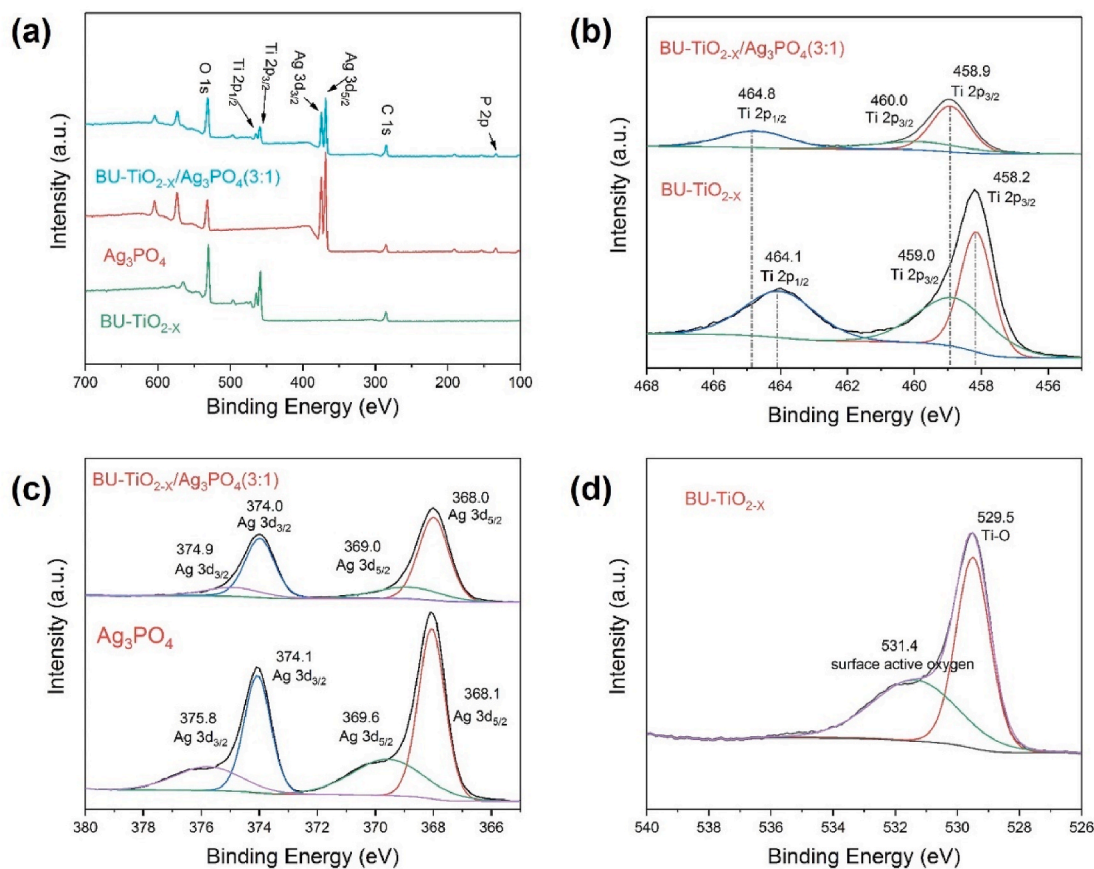

Fig. 2. The micromorphology, crystal structure, and phase composition of synthesized materials: (a) TEM images (Scale bar: 20 nm) and (b) HRTEM images (Scale bar: 2 nm) of U–TiO_2, BU-TiO_{2-X} and BU-TiO_{2-X}/Ag_3PO_4(3:1); (c)XRD patterns of U–TiO_2, BU-TiO_{2-X}, Ag_3PO_4 and BU-TiO_{2-X}/Ag_3PO_4 (6:1, 3:1, 1:1); (d) Raman spectroscopy of U–TiO_2, BU-TiO_{2-X}.

Fig. 3. (a)XPS survey spectrum of BU-TiO$_{2-X}$, Ag$_3$PO$_4$, and BU-TiO$_{2-X}$/Ag$_3$PO$_4$ (3:1); (b) High-resolution scans for Ti 2p electrons of the BU-TiO$_{2-X}$ and BU-TiO$_{2-X}$/Ag$_3$PO$_4$ (3:1); (c) High-resolution scans for Ag 3d electrons of Ag$_3$PO$_4$ and BU-TiO$_{2-X}$/Ag$_3$PO$_4$ (3:1); (d) High-resolution scans for O 1s electrons of BU-TiO$_{2-X}$.

oxygen vacancy) formed on the surface of BU- TiO$_{2-X}$ [67]. And the intensity of the BU-TiO$_{2-X}$ peaks decreased and broadened after the reduction process by NaBH$_4$ because the oxygen vacancies decrease the oxygen atom vibration frequency, indicating that the vibration of the O atom is in connection with oxygen defects [68].

XPS analysis was further carried out to determine the elemental composition and chemical states of the synthesized samples. As shown in Fig. 3(a), the peaks of Ag, P, C, Ti, and O were detected in the BU-TiO$_{2-X}$/Ag$_3$PO$_4$ (3:1) while only C, Ti, and O were found in the BU-TiO$_{2-X}$. In addition, the signal intensity of Ag 3d and Ti 2p detected from the hybrid was lower than the corresponding intensity found in the single component, suggesting that the hybrid was successfully prepared. As shown in Fig. 3(b), the high-resolution scan of Ti 2p, detected from the BU-TiO$_{2-X}$ and BU-TiO$_{2-X}$/Ag$_3$PO$_4$, indicated that Ti 2p contained peaks of Ti 2p$_{1/2}$ at 464.2 eV, Ti 2p$_{1/2}$ at 464.8 eV, Ti 2p$_{3/2}$ at 458.3 eV, and Ti 2p$_{3/2}$ at 458.9 eV, which belonged to the Ti^{4+} [69,70]. Compared to BU-TiO$_{2-X}$, the peaks of the BU-TiO$_{2-X}$/Ag$_3$PO$_4$ (3:1) sample showed a positive shift in binding energy, indicating an interfacial interaction between Ag$_3$PO$_4$ and BU-TiO$_{2-X}$. This could be ascribed to the formation of Ti–O–P bonds, which were beneficial for reducing the recombination of the photogenerated electron–hole pairs [58,71,72]. As shown in Fig. 3(c), the high-resolution spectra of Ag 3d, obtained from the Ag$_3$PO$_4$ and BU-TiO$_{2-X}$/Ag$_3$PO$_4$ (3:1), showed that Ag 3d contained peaks of Ag 3d$_{3/2}$ at 374.0 eV, Ag 3d$_{3/2}$ at 374.1 eV, Ag 3d$_{5/2}$ at 368.0 eV and Ag 3d$_{5/2}$ at 368.1 eV, which belonged to the Ag$^+$ [73]. The Ag 3d also contained peaks of Ag 3d$_{3/2}$ at 375.8 eV, Ag 3d$_{3/2}$ at 374.9 eV, Ag 3d$_{5/2}$ at 369.6 eV, and Ag 3d$_{5/2}$ at 369.0 eV, which belonged to the Ag^0 [73,74]. Compared with Ag$_3$PO$_4$, the peaks of the Ag^0 in the BU-TiO$_{2-X}$/-Ag$_3$PO$_4$ (3:1) sample showed a negative shift in binding energy and a lower intensity, suggesting that the formation of the BU-TiO$_{2-X}$/Ag$_3$PO$_4$ hybrid can prevent Ag$^+$ from becoming Ag^0 [74,75]. In Fig. 3(d), the

main peak of O 1s, centered at 529.5 eV, could have been caused by oxygen lattices in BU-TiO$_{2-X}$. The peak at 531.4 eV for BU-TiO$_{2-X}$ was also ascribed to surface active oxygen that was chemisorbed by oxygen defects (such as oxygen vacancy) [76]. In addition, the atom percentages of Ti and O could be measured using peak areas and the relative sensitivity factor. The stoichiometric ratio of the O$_{Ti}$(O–Ti): Ti$_{2p}$ atoms in the BU-TiO$_{2-X}$ sample was 1.88:1, indicating the appearance of oxygen vacancies after the NaBH$_4$ reduction process [77,78]. These results further demonstrated that Ag$_3$PO$_4$ had been successfully combined with the BU-TiO$_{2-X}$, which is in line with the XRD results.

3.2. Photocatalytic property

Fig. 4(a) presents the UV–Vis absorption spectra of the synthesized samples. The UV–Vis spectrum of the Ag$_3$PO$_4$ sample indicated that it absorbed sunlight with a wavelength less than 532 nm, corresponding to 2.33 eV of the bandgap energy [19]. The U–TiO$_2$ exhibited an absorption tail of less than 390 nm in the ultraviolet light region, corresponding to 3.20 eV of the bandgap energy. These results are in agreement with previous reports [61,64]. Compared to U–TiO$_2$, BU-TiO$_{2-X}$ exhibited a much wider absorption range, from 410 nm to 800 nm, corresponding to 2.72 eV of the bandgap energy (Fig. 4(b)). The edge potentials of the conduction band (CB) and the valence band (VB) of the photocatalysts could be calculated according to Eqs. (3) and (4) [79–81].

$$E_{VB} = \chi - E_e + 1/2E_g \qquad (3)$$

$$E_{CB} = E_{VB} - E_g \qquad (4)$$

where χ means the absolute electronegativity of the photocatalysts, which can be calculated from the geometric mean of the electronegativity in the constituent atoms (5.75 eV for BU-TiO$_{2-X}$ and 5.96 eV for
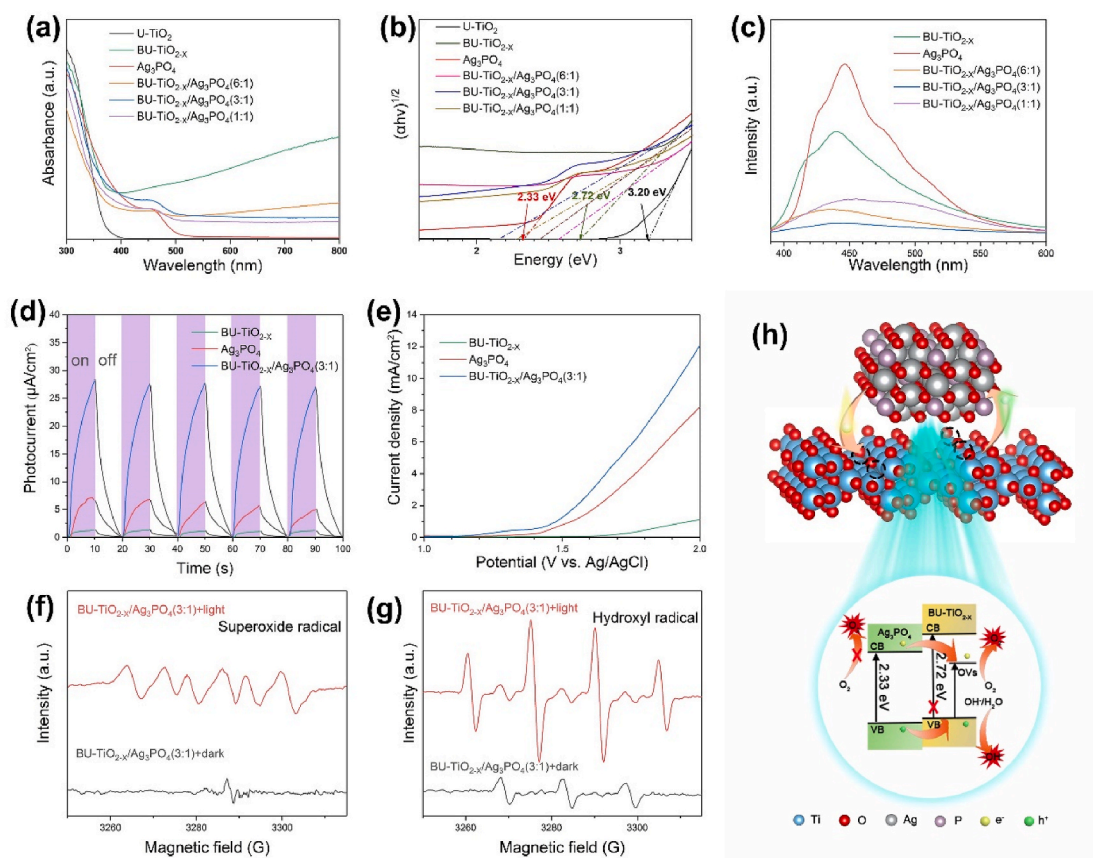
Fig. 4. (a) The UV–vis–NIR absorption curves and (b) band energy gap of synthesized materials; (c) Steady state photoluminescence spectra of U– TiO_2, BU-TiO_{2-x}, Ag_3PO_4, and BU-TiO_{2-x}/Ag_3PO_4 (3:1); (d) photocurrent curves and (e) linear voltammetry sweep photocurrent curves of BU-TiO_{2-x}, Ag_3PO_4 and BU-TiO_{2-x}/Ag_3PO_4 (3:1) under visible light irradiation; ESR spectra of (f) superoxide radical, and (g) hydroxyl radical, obtained from BU-TiO_{2-x}/Ag_3PO_4 (3:1); (h) The schematic illustration of the photocatalytic mechanism of BU-TiO_{2-x}/Ag_3PO_4 heterostructure under visible light.

Ag_3PO_4) [80]. E_g and E_e are the bandgap values of the photocatalyst and the energy of free electrons, with a value of 4.5 eV (*vs* Normal Hydrogen Electrode [NHE]). From the above, the calculated CB and VB potential of the synthesized BU-TiO_{2-X} and Ag_3PO_4 were −0.11 eV, 2.61 eV and 0.30 eV, 2.63 eV *vs* NHE, respectively. For the BU-TiO_{2-X}/Ag_3PO_4 (6:1, 3:1, 1:1) samples, the absorption spectra not only exhibited a larger characteristic absorption band edge, but also had a better absorption intensity in the visible region. In fact, BU-TiO_{2-X} enabled the transfer of some photogenerated electrons from Ag_3PO_4 to BU-TiO_{2-X} because of the oxygen deficiency on the surface of BU-TiO_{2-X}, thus inhibiting electron–hole recombination and enhancing the photocatalytic ability.

Fig. 4(c) shows the PL spectra of the synthesized samples, which can be used to perceive the recombination and separation efficiency of the photogenerated electron–hole pairs. The intensity of PL emission from the BU-TiO_{2-X}/Ag_3PO_4 (6:1, 3:1, 1:1) at about 445 nm was far below that of BU-TiO_{2-X} and Ag_3PO_4, indicating that the combination of BU-TiO_{2-X} and Ag_3PO_4 is beneficial to the separation of photogenerated electron–hole pairs, which can endow the hybrid with better photocatalytic performance than that of BU-TiO_{2-X} or Ag_3PO_4 alone. Moreover, the BU-TiO_{2-X}/Ag_3PO_4 (3:1) showed the lowest intensity of PL emission among three kinds of hybrids. When the molar ratio between BU-TiO_{2-X} and Ag_3PO_4 is 6:1, the bandgap is further larger than that of other composites, leading to a lower charge excitation efficiency; when the molar ratio between BU-TiO_{2-X} and Ag_3PO_4 is 1:1, the PL intensity is higher than that of other composites, leading to faster recombination of photogenerated electron–hole pairs. In brief, the molar ratio between BU-TiO_{2-X} and Ag_3PO_4 plays a critical role in effectively accelerating charge transfer and inhibiting the recombination of photogenerated electron–hole pairs.

Both transient photocurrent response and linear sweep voltammetry (LSV) are significant photoelectrochemical measurements for better understanding electron transfer and separation in the samples under visible light irradiation. As seen in Fig. 4(d), the BU-TiO_{2-X}, Ag_3PO_4, and BU-TiO_{2-X}/Ag_3PO_4 (3:1) samples had five repeated photocurrent responses over time (I–t)—on/off cycles, with and without the irradiation of simulated solar light (Xenon lamp light, 0.2 W cm^{-2}). Under the light irradiation, BU-TiO_{2-X}/Ag_3PO_4 (3:1) exhibited the strongest photocurrent, which was far higher than the photocurrents of Ag_3PO_4 or BU-TiO_{2-X} alone. The current density *vs* the potential (J–V) of the synthesized samples was measured under the irradiation of Xenon lamplight with the same power. As Fig. 4(e) indicates, the current density of BU-TiO_{2-X}/Ag_3PO_4 (3:1) was obviously higher than those of BU-TiO_{2-X} and Ag_3PO_4, which was well in accordance with the PL results, suggesting that the synthesized hybrid had a much stronger photocatalytic performance. This enhanced photocatalytic performance indicates that photocatalysts can produce more ROS after absorbing photons in appropriate environments, which can endow the material with better antibacterial activity. The electron spin resonance (ESR) spectrum can be used to evaluate the ROS yields of photocatalysts under light irradiation. As shown in Fig. 4(f), obvious six-line peaks were observed, indicating the formation of •O_2^- [82]. The strong characteristic peaks, with an intensity ratio of 1:2:2:1, are displayed in Fig. 4(g), suggesting the production of large amount of •OH [52]. The above results demonstrated that BU-TiO_{2-X}/Ag_3PO_4 (3:1) can produce •OH and •O_2^- under visible light irradiation [15]. The photocatalytic mechanism of the BU-TiO_{2-X}/-Ag_3PO_4 hybrid for generating ROS is schematically illustrated in Fig. 4 (h). BU-TiO_{2-X}/Ag_3PO_4 (3:1) is excited to generate electrons and holes under visible light irradiation. The oxygen vacancy of U–TiO_{2-X},

produced by $NaBH_4$ reduction, leads to local states below the conduction band edge [13], and acts as an electron acceptor to inhibit the recombination of photo-generated charges in BU-TiO_{2-X}/Ag_3PO_4 (3:1) [48], consequently enhancing the photocatalysis of BU-TiO_{2-X}/Ag_3PO_4 (3:1). According to the CB and VB potential of synthesized BU-TiO_{2-X} and Ag_3PO_4, the oxygen vacancy in BU-TiO_{2-X}/Ag_3PO_4 (3:1) can retard the flow of electrons to Ag^+, thus preventing the Ag^+ of Ag_3PO_4 from forming Ag^0 compared to Ag_3PO_4 alone [19], which is in keeping with the XPS results.

3.3. In vitro antibacterial activity

The spread plate results in Fig. S3 present the antibacterial capability of the synthesized samples against *E. coli* and *S. aureus*. In Fig. S3(a), it is obvious that there was almost no reduction in *E. coli* colonies among the synthesized samples compared to that of the control in the dark, indicating that none of the samples had antibacterial activity against *E. coli* without light irradiation for 20 min. Under the irradiation of Xenon lamp light, the BU-TiO_{2-X} samples exhibited little antibacterial activity, but it was evident that the nanospikes and photodynamic effect of BU-TiO_{2-X} did have some influence on *E. coli* in the short term. In contrast, under light irradiation, all Ag_3PO_4 containing samples, due to their photocatalytic properties, reduced bacterial colonies at different levels compared to the control. However, almost no bacterial colonies remained in the group of BU-TiO_{2-X}/Ag_3PO_4 (3:1) group, suggesting that it had the best antibacterial efficacy against *E. coli* because of its strongest photocatalytic performance. Under the same conditions, the antibacterial activity of all synthesized samples against *S. aureus* exhibited the same trends as against *E. coli* (Fig. S3(b)). The calculated antibacterial efficiencies against *E. coli* and *S. aureus* are shown in Fig. 5(a) and (b). The BU-TiO_{2-X}/Ag_3PO_4 (3:1) sample had the highest antibacterial efficiencies (99.73 ± 0.18% and 98.10 ± 0.09%) against *E. coli* and *S. aureus*, respectively, under visible light irradiation for 20 min. This was followed by Ag_3PO_4, BU-TiO_{2-X}/Ag_3PO_4 (6:1), and BU-TiO_{2-X}/Ag_3PO_4 (1:1), with corresponding antibacterial efficiencies of 90.1 ± 1.65%, 95.31 ± 1.17%, 82.58 ± 0.9% against *E. coli* and 56.85 ± 3.39%,

81.68 ± 1.8%, 89.08 ± 3.09% against *S. aureus*, respectively. The physical puncture administered by the BU-TiO_{2-X} and the Ag^+ released from the Ag_3PO_4 played significant roles in the samples' antibacterial activity against *E. coli* and *S. aureus*, as proven by culturing the bacteria with the samples in the dark for 12 h (Figs. S3(c) and 5(c)). The long-term antibacterial efficiency of BU-TiO_{2-X}/Ag_3PO_4 (3:1) was superior to BU-TiO_{2-X} or Ag_3PO_4 alone, and, after visible light irradiation for 20 min, the BU-TiO_{2-X}/Ag_3PO_4 (3:1) sample had the highest long-term antibacterial efficiency of 99.76 ± 0.15% and 99.85 ± 0.09% against *E. coli* and *S. aureus*, respectively, in the dark for 12 h. In addition, the combination of BU-TiO_{2-X} and Ag_3PO_4 suppressed Ag^+ leaching from Ag_3PO_4 (Fig. 5(d)), indicating that the increasing antibacterial efficiency of the BU-TiO_{2-X}/Ag_3PO_4 hybrid may be ascribed to physical puncture administered by BU-TiO_{2-X}. The inactivation kinetics of *E. coli* and *S. aureus* in the BU-TiO_{2-X}/Ag_3PO_4 (3:1) sample were investigated via Xenon lamplight in Fig. 5(e) and (f). The antibacterial efficiency of the BU-TiO_{2-X}/Ag_3PO_4 (3:1) sample against *E. coli* was obviously higher than that against *S. aureus* after light irradiation for 15 min. These antibacterial results are mainly ascribed to the samples' photocatalytic performance, physical structure, and Ag^+ release, which will be discussed below in the antibacterial mechanism section.

As shown in Fig. 6, bacterial microcosmic morphologies were observed via SEM, the ultrathin sectional TEM images, and the corresponding EDS. After visible light irradiation for 20 min (Fig. 6(a) and (b)), the *E. coli* and *S. aureus* cells had intact cell walls with smooth surfaces and full cytoplasm in the control (without samples or light). With respect to the BU-TiO_{2-X} sample, there were some depressed areas on the bacterial membranes and complete cell walls. In contrast, the *E. coli* exposed to the Ag_3PO_4 sample were evidently deformed. Spots of the bacterial membranes had ruptured, and their inner materials had flowed out; however, the bacterial membranes of *S. aureus* did not rupture. The membranes of most *E. coli* and *S. aureus* cells were broken, and the inner content had flowed out, when the cells were exposed to the BU-TiO_{2-X}/Ag_3PO_4 (3:1) sample. With the BU-TiO_{2-X} sample, after remaining in the dark for 12 h (Fig. 6(c)), the membranes of the *E. coli* and *S. aureus* cells showed puncture marks, while the BU-TiO_{2-X}/Ag_3PO_4
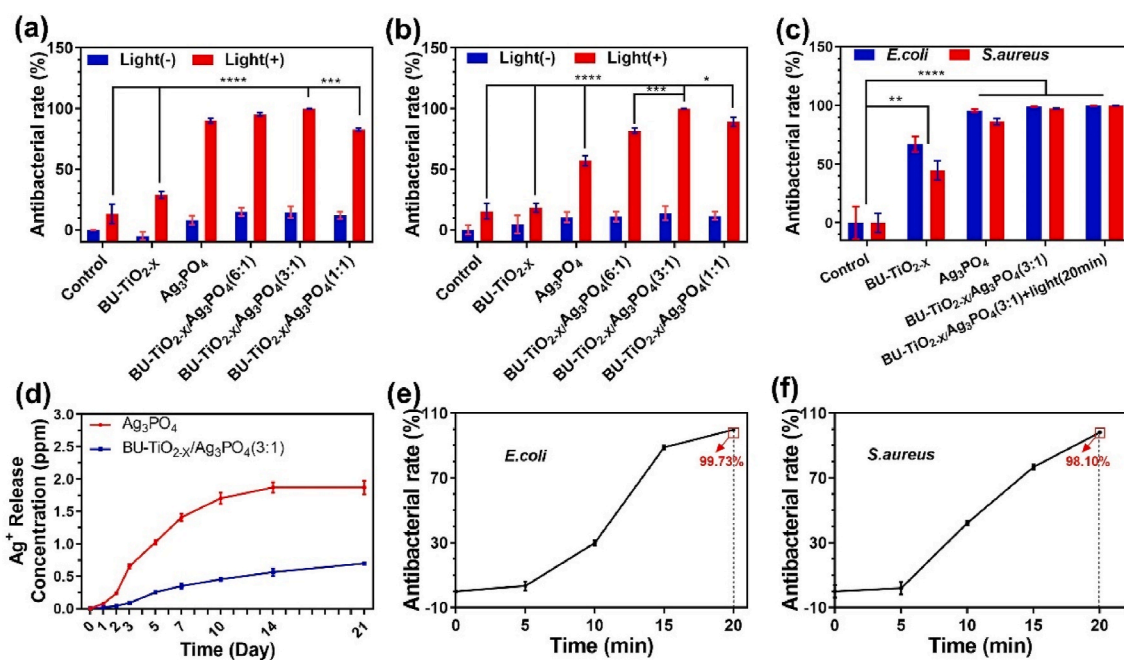

Fig. 5. The antibacterial activities of the synthesized samples. The antibacterial efficiency of the synthesized samples against (a) *E. coli* and (b) *S. aureus* after light irradiation or staying in dark for 20 min; (c) the antibacterial efficiency of the synthesized samples against *E. coli* and *S. aureus* after staying in dark for 12 h; (d) long-term release of Ag ions from Ag_3PO_4 and BU-TiO_{2-X}/Ag_3PO_4 in 100 mL of DI water (PH = 7.4) at 37 °C; the antibacterial kinetics of (e) *E. coli* and (f) *S. aureus* for BU-TiO_{2-X}/Ag_3PO_4 (3:1) under visible light. The error bars indicate means ± SD, n = 3. *p < 0.05, **p < 0.01, ***p < 0.001, ****p < 0.0001.
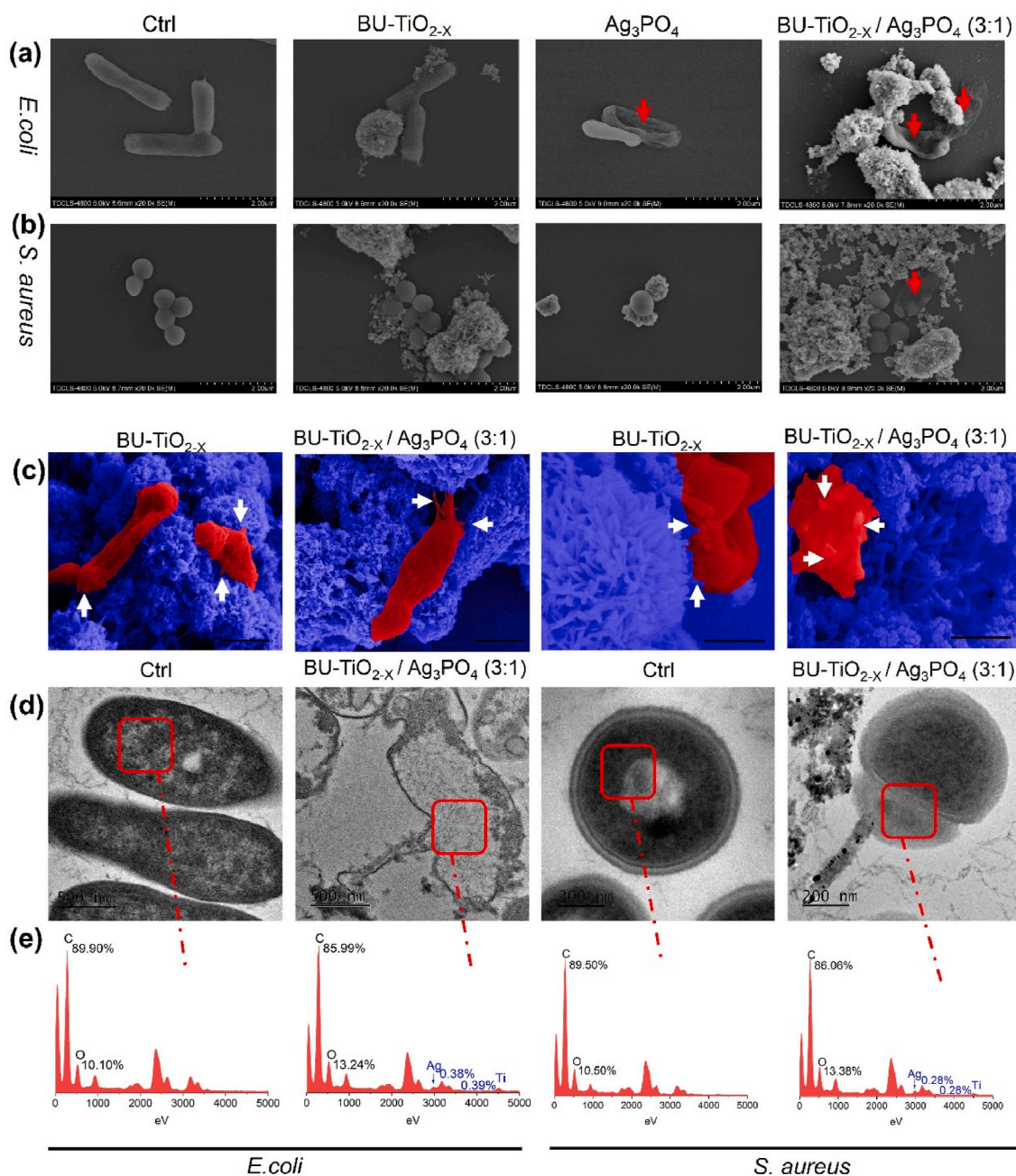
Fig. 6. The FE-SEM and TEM images of bacteria. (a) *E. coli* and (b) *S. aureus* after irradiation by visible light or staying in dark for 20 min; (c) *E. coli* and *S. aureus* after staying in dark for 12 h (Scale bar: 500 nm); (d) TEM images of ultrathin section and (e) the corresponding EDS of *E. coli* and *S. aureus*.

(3:1) sample very obviously ripped and punctured the membranes of both bacterial types. In addition, the ultrathin sectional TEM images and the corresponding EDS (Fig. 6(d) and (e)) further showed the puncturing behavior of BU-TiO$_{2-X}$/Ag$_3$PO$_4$ (3:1). In the control, the *E. coli* and *S. aureus* cells both retained normal-shaped structures with intact bacterial membranes, and EDS showed no signs of Ti or Ag, while the nanospikes on the BU-TiO$_{2-X}$/Ag$_3$PO$_4$ (3:1) held tight contact with the *E. coli* and *S. aureus* cells and even visibly deformed the *E. coli* cells. The corresponding EDS results also demonstrated that a small amount of ionic Ti and Ag penetrated the *E. coli* and *S. aureus* cells, which further proved that BU-TiO$_{2-X}$/Ag$_3$PO$_4$ (3:1) can puncture the cell membranes. As mentioned above, these results and the spread plate findings corroborated well.

3.4. Computational modeling of cell membrane puncture

Activation energy theory can be used to describe cell membrane puncture [83]. According to previous research, the rupture of the cell membrane depends on the free energy of deformed cells. When the free energy per unit area is larger than the threshold value [$(2.9–8.3) \times 10^{-3}$ J/m^2], cell membrane puncture occurs [53,84]. In the following simulation, the researchers chose the minimum threshold value (2.9×10^{-3} J/m^2) as the critical value according to their experimental results. Considering the nanospikes on the surface of the BU-TiO$_{2-X}$ in all directions, the authors simulated the free energy variety of *E. coli* and *S. aureus* cells with a nanospike at different angles. At the same time, they assumed that angle(θ) was 0° when the nanospike was perpendicular to the *E. coli* or *S. aureus* cells. It is worth noting that when θ goes beyond around 65° for *E. coli* and around 50° for *S. aureus*, the

bacteria–nanospike system is unstable, and the simulation does not converge. As shown in Fig. 7(a), compared to being punctured with a nanospike at 0°, the *E. coli* cell generated a higher free energy density of 3.31×10^{-3} J/m^2 at 45°. The membrane deformation of the *E. coli* cell at 45° (outlined by the red circle) is visibly larger than 0°. Under the same simulated condition, the free energy density and membrane deformation of *S. aureus* exhibited the same trend as *E. coli* (Fig. 7(b)). The density distribution of the bacterial free energy and the membrane deformation for *E. coli* and *S. aureus* at each angle are shown in Movies 1 and 2. The free energy value increased as the angle increased for both *E. coli* and *S. aureus* (Fig. 7(c)). A puncture criterion (free energy density = 2.9×10^{-3} Jm^{-2}) separated the free energy density–angle plane into green (punctured) and blank regions. Compared to *S. aureus*, *E. coli* reached the free energy threshold at about 32°–11° lower than *S. aureus*. The difference in deformation was further proved by the bacteria's corresponding penetration depth results (Fig. 7(d)). The penetration depth for the *E. coli* cells was greater than that for *S. aureus*, indicating that *E. coli* cells are susceptible to the nanospikes, which is in line with the spread plate results.

3.5. Antibacterial mechanism

The above results demonstrate that the BU-TiO$_{2-X}$/Ag$_3$PO$_4$ hybrid had better antibacterial activity against *E. coli* and *S. aureus*. The antibacterial mechanisms of the BU-TiO$_{2-X}$/Ag$_3$PO$_4$ hybrid have three aspects, which are shown in Scheme 2 [52, 58, 85], as follows. (A) ROS (Fig. 4(f) and (g)), such as •OH and •O$_2^-$, are generated by the BU-TiO$_{2-X}$/Ag$_3$PO$_4$ hybrid under visible light; they can disrupt the cell membrane (Fig. 6(a) and (b)) and induce oxidative stress, which causes cell death. (B) Silver ions (Fig. 5(d)), released by the Ag$_3$PO$_4$ NPs, can penetrate cell membranes to inhibit active transport and bacterial metabolism when the concentration reaches a certain level. (C) BU-TiO$_{2-X}$ NPs can puncture bacterial cell walls, leading to deformation and even rupture of the bacterial membranes which causes bacterial death (Fig. 6(c) and (d)). The intense nanospikes, with a mean diameter of 20 nm, on the surface of the BU-TiO$_{2-X}$ NPs provide enough "arms" in all directions.

3.6. In vitro cytotoxicity test

As shown in Fig. S4, the Cell Counting Kit-8 (cck-8) assay evaluated cell viabilities on different leach liquors after one, three, and five days of incubation, since the Ag$^+$ released by Ag$_3$PO$_4$ NPs have higher toxicity than Ag NPs according to previous research [86]. Without visible light irradiation, the cell viability of the Ag$_3$PO$_4$ sample was lower than that of the BU-TiO$_{2-X}$/Ag$_3$PO$_4$ (3:1) sample at the first day. However, the cell viability of the Ag$_3$PO$_4$ sample was obviously higher than that of the BU-TiO$_{2-X}$/Ag$_3$PO$_4$ (3:1) sample by the third day, suggesting that Ag$_3$PO$_4$ was less stable in water than BU-TiO$_{2-X}$/Ag$_3$PO$_4$ (3:1). At the fifth day, the cell viability of the Ag$_3$PO$_4$ and BU-TiO$_{2-X}$/Ag$_3$PO$_4$ (3:1) samples both approximated that of the control sample, indicating that, while Ag$_3$PO$_4$ and BU-TiO$_{2-X}$/Ag$_3$PO$_4$ (3:1) presented some toxicity in the short term, their cell viability was enhanced and close to 95% in the long term. Thus, the CCK-8 assay proved that BU-TiO$_{2-X}$/Ag$_3$PO$_4$ (3:1) had good biocompatibility *in vitro*.
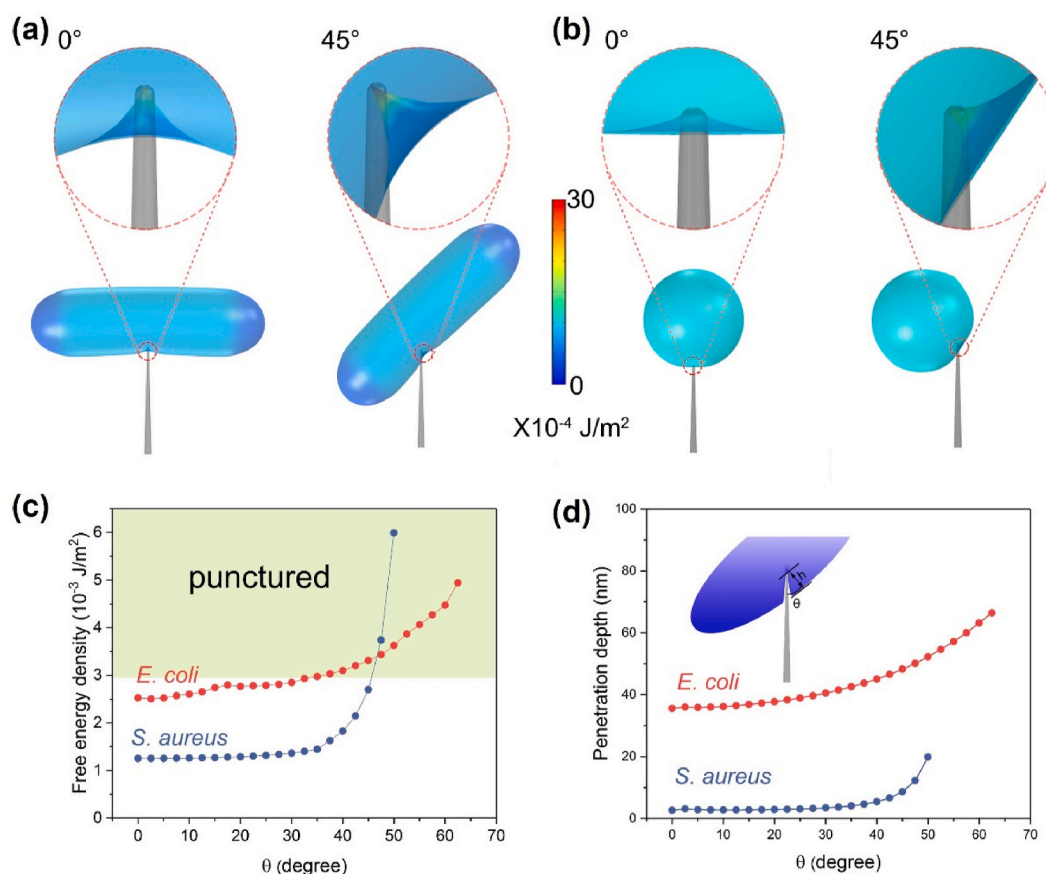
Fig. 7. Computational modeling of cell membrane penetration. The density distribution of bacterial free energy and membrane deformation as the bacteria deform on the nanospikes (d = 20 nm) with two kinds of angles (θ): θ = 0° and θ = 45° for (a) *E. coli* and (b) *S. aureus*; (c) the maximum value of bacterial free energy density of *E. coli* and *S. aureus* cell punctured by nanospikes rises with increasing θ; (d) The penetration depth of *E. coli* and *S. aureus* cell with various θ.
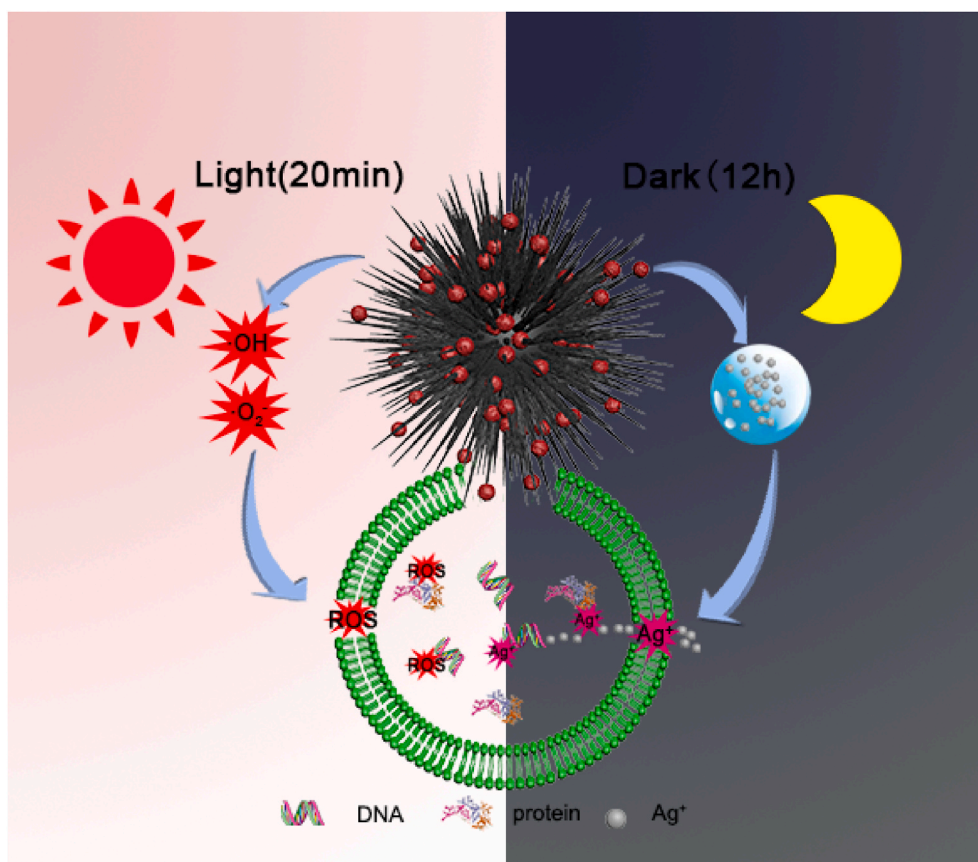
Scheme 2. Schematic illustration of possible photocatalysis, physical puncture and released Ag^+ mechanisms of BU-TiO$_{2-x}$/Ag$_3$PO$_4$ heterostructure.

4. Conclusions

BU-TiO$_{2-X}$/Ag$_3$PO$_4$, with various molar ratio, is controllably designed to enhance its photodynamic therapeutic efficacy to combat *E. coli* or *S. aureus* infections through the synergistic antibacterial effects of ROS, nanospikes, and Ag^+ release. The cooperation of BU-TiO$_{2-X}$ and Ag$_3$PO$_4$ can decrease their bandgap, inhibit the recombination of photogenerated electron–hole pairs, and effectively promote charge transfer. BU-TiO$_{2-X}$/Ag$_3$PO$_4$ may have an optimum molar ratio of 3:1 which showed the best antibacterial efficiency (99.76 $\pm$ 0.15% and 99.85 $\pm$ 0.09%) against *E. coli* and *S. aureus* after 20 min of light irradiation followed by darkness for 12 h. The BU-TiO$_{2-X}$/Ag$_3$PO$_4$ (3:1) heterojunction have great antibacterial efficacy rapidly under visible light. Meanwhile, the physical puncture administered by the nanospikes on the surface of BU-TiO$_{2-X}$, combined with the Ag^+ released by Ag$_3$PO$_4$, have long-term bacteriostatic efficacy. Consequently, BU-TiO$_{2-X}$/Ag$_3$PO$_4$ has great potential for eliminating infections rapidly and effectively.

CRediT authorship contribution statement

Yingde Xu: Conceptualization, Methodology, Data curation, Writing - original draft. **Xiangmei Liu:** Conceptualization, Writing - review & editing, Supervision, Project administration. **Yufeng Zheng:** Conceptualization, Supervision, Project administration. **Changyi Li:** Methodology. **Kelvin Wai Kwok Yeung:** Methodology. **Zhenduo Cui:** Methodology. **Yanqin Liang:** Methodology. **Zhaoyang Li:** Methodology. **Shengli Zhu:** Methodology. **Shuilin Wu:** Conceptualization, Writing - review & editing, Supervision, Project administration.

Declaration of competing interest

The authors declare that they have no competing interests.

Appendix A. Supplementary data

Supplementary data to this article can be found online at https://doi.org/10.1016/j.bioactmat.2020.11.013.

References

[1] B.M. Hover, S.H. Kim, M. Katz, Z. Charlop-Powers, J.G. Owen, M.A. Ternei, J. Maniko, A.B. Estrela, H. Molina, S. Park, D.S. Perlin, S.F. Brady, Culture-independent discovery of the malacidins as calcium-dependent antibiotics with activity against multidrug-resistant Gram-positive pathogens, Nat. Microbiol. 3 (4) (2018) 415–422.

[2] K. Lewis, Platforms for antibiotic discovery, Nat. Rev. Drug Discov. 12 (5) (2013) 371–387.

[3] S. Baker, N. Thomson, F.X. Weill, K.E. Holt, Genomic insights into the emergence and spread of antimicrobial-resistant bacterial pathogens, Science 360 (6390) (2018) 733.

[4] M.P. Paudyal, A.M. Adebesin, S.R. Burt, D.H. Ess, Z. Ma, L. Kurti, J.R. Falck, Dirhodium-catalyzed C-H arene amination using hydroxylamines, Science 353 (6304) (2016) 1144–1147.

[5] J. Li, X. Liu, L. Tan, Y. Liang, Z. Cui, X. Yang, S. Zhu, Z. Li, Y. Zheng, K.W.K. Yeung, X. Wang, S. Wu, Light-activated rapid disinfection by accelerated charge transfer in red phosphorus/ZnO heterointerface, Small Methods 3 (3) (2019) 1900048.

[6] L. Tan, J. Li, X. Liu, Z. Cui, X. Yang, S. Zhu, Z. Li, X. Yuan, Y. Zheng, K.W.K. Yeung, H. Pan, X. Wang, S. Wu, Rapid biofilm eradication on bone implants using red phosphorus and near-infrared light, Adv. Mater. 30 (31) (2018) 1801808.

[7] T. Wei, Q. Yu, H. Chen, Responsive and synergistic antibacterial coatings: fighting against bacteria in a smart and effective way, Adv. Healthcare Mater. 8 (3) 2019 1801381.

[8] J. Xu, X. Cheng, L. Tan, C. Fu, M. Ahmed, J. Tian, J. Dou, Q. Zhou, X. Ren, Q. Wu, S. Tang, H. Zhou, X. Meng, J. Yu, P. Liang, Microwave responsive nanoplatform via P-selectin mediated drug delivery for treatment of hepatocellular carcinoma with distant metastasis, Nano Lett. 19 (5) (2019) 2914–2927.

[9] X. Qian, Y. Zheng, Y. Chen, Micro/nanoparticle-augmented sonodynamic therapy (SDT): breaking the depth shallow of photoactivation, Adv. Mater. 28 (37) (2016) 8097–8129.

[10] Y. Ren, Y. Han, Z. Li, X. Liu, S. Zhu, Y. Liang, K.W.K. Yeung, S. Wu, Ce and Er co-doped TiO_2 for rapid bacteria-killing using visible light, Bioact. Mater. 5 (2) (2020) 201–209.

[11] D.O. Scanlon, C.W. Dunnill, J. Buckeridge, S.A. Shevlin, A.J. Logsdail, S. M. Woodley, C.R. Catlow, M.J. Powell, R.G. Palgrave, I.P. Parkin, G.W. Watson, T. W. Keal, P. Sherwood, A. Walsh, A.A. Sokol, Band alignment of rutile and anatase TiO_2, Nat. Mater. 12 (9) (2013) 798–801.

[12] H. Ji, L. Lyu, L. Zhang, X. An, C. Hu, Oxygen vacancy enhanced photostability and activity of plasmon-Ag composites in the visible to near-infrared region for water purification, Appl. Catal., B 199 (2016) 230–240.

[13] X. Pan, M.Q. Yang, X. Fu, N. Zhang, Y.J. Xu, Defective TiO_2 with oxygen vacancies: synthesis, properties and photocatalytic applications, Nanoscale 5 (9) (2013) 3601–3614.

[14] E.L. Zhang, S. Fu, R.X. Wang, H.X. Li, Y. Liu, Z.Q. Ma, G.K. Liu, C.S. Zhu, G.W. Qin, D.F. Chen, Role of Cu element in biomedical metal alloy design, Rare Met. 38 (6) (2019) 476–494.

[15] K. Su, L. Tan, X. Liu, Z. Cui, Y. Zheng, B. Li, Y. Han, Z. Li, S. Zhu, Y. Liang, X. Feng, X. Wang, S. Wu, Rapid photo-sonotherapy for clinical treatment of bacterial infected bone implants by creating oxygen deficiency using sulfur doping, ACS Nano 14 (2) (2020) 2077–2089.

[16] K. Dai, J. Lv, J. Zhang, G. Zhu, L. Geng, C. Liang, Efficient visible-light-driven splitting of water into hydrogen over surface-fluorinated anatase TiO_2 nanosheets with exposed {001} facets/layered CdS–diethylenetriamine nanobelts, ACS Sustain. Chem. Eng. 6 (10) (2018) 12817–12826. Submitted for publication.

[17] J. Lv, J. Zhang, J. Liu, Z. Li, K. Dai, C. Liang, Bi SPR-promoted Z-scheme Bi_2MoO_6/CdS-diethylenetriamine composite with effectively enhanced visible light photocatalytic hydrogen evolution activity and stability, ACS Sustain. Chem. Eng. 6 (1) (2017) 696–706.

[18] K. Dai, L. Lu, C. Liang, Q. Liu, G. Zhu, Heterojunction of facet coupled g-C_3N_4/surface-fluorinated TiO_2 nanosheets for organic pollutants degradation under visible LED light irradiation, Appl. Catal., B 156–157 (2014) 331–340.

[19] Z. Yi, J. Ye, N. Kikugawa, T. Kako, S. Ouyang, H. Stuart-Williams, H. Yang, J. Cao, W. Luo, Z. Li, Y. Liu, R.L. Withers, An orthophosphate semiconductor with photooxidation properties under visible-light irradiation, Nat. Mater. 9 (7) (2010) 559–564.

[20] X. Ma, H. Li, Y. Wang, H. Li, B. Liu, S. Yin, T. Sato, Substantial change in phenomenon of "self-corrosion" on Ag_3PO_4/TiO_2 compound photocatalyst, Appl. Catal., B 158 (2014) 314–320.

[21] Y. Chai, Y. Ding, L. Wang, Q. Liu, J. Ren, W.L. Dai, Enormous enhancement in photocatalytic performance of Ag_3PO_4/HAp composite: a Z-scheme mechanism insight, Appl. Catal., B 179 (2015) 29–36.

[22] Y. Bi, S. Ouyang, N. Umezawa, J. Cao, J. Ye, Facet effect of single-crystalline Ag_3PO_4 sub-microcrystals on photocatalytic properties, J. Am. Chem. Soc. 133 (17) (2011) 6490–6492.

[23] Y. Bi, S. Ouyang, J. Cao, J. Ye, Facile synthesis of rhombic dodecahedral AgX/Ag_3PO_4 (X = Cl, Br, I) heterocrystals with enhanced photocatalytic properties and stabilities, Phys. Chem. Chem. Phys. 13 (21) (2011) 10071–10075.

[24] N. Shao, J. Wang, D. Wang, P. Corvini, Preparation of three-dimensional Ag_3PO_4/TiO_2@MoS_2 for enhanced visible-light photocatalytic activity and anti-photocorrosion, Appl. Catal., B 203 (2017) 964–978.

[25] L. Hong, X. Liu, L. Tan, Z. Cui, X. Yang, Y. Liang, Z. Li, S. Zhu, Y. Zheng, K. K. Yeung, D. Jing, D. Zheng, X. Wang, S. Wu, Rapid biofilm elimination on bone implants using near-infrared-activated inorganic semiconductor heterostructures, Adv. Healthcare Mater. 8 (19) (2019), 1900835.

[26] Z. Wang, T. Hu, K. Dai, J. Zhang, C. Liang, Construction of Z-scheme Ag_3PO_4/Bi_2WO_6 composite with excellent visible-light photodegradation activity for removal of organic contaminants, Chin. J. Catal. 38 (12) (2017) 2021–2029.

[27] H. Wang, L. Zhang, Z. Chen, J. Hu, S. Li, Z. Wang, J. Liu, X. Wang, Semiconductor heterojunction photocatalysts: design, construction, and photocatalytic performances, Chem. Soc. Rev. 43 (15) (2014) 5234–5244.

[28] P. Tan, X. Chen, L. Wu, Y.Y. Shang, W. Liu, J. Pan, X. Xiong, Hierarchical flower-like $SnSe_2$ supported Ag_3PO_4 nanoparticles: towards visible light driven photocatalyst with enhanced performance, Appl. Catal., B 202 (2017) 326–334.

[29] F. Chen, Q. Yang, X. Li, G. Zeng, D. Wang, C. Niu, J. Zhao, H. An, T. Xie, Y. Deng, Hierarchical assembly of graphene-bridged Ag_3PO_4/Ag/$BiVO_4$ (040) Z-scheme photocatalyst: an efficient, sustainable and heterogeneous catalyst with enhanced visible-light photoactivity towards tetracycline degradation under visible light irradiation, Appl. Catal., B 200 (2017) 330–342.

[30] P. Zhou, J. Yu, M. Jaroniec, All-solid-state z-scheme photocatalytic systems, Adv. Mater. 26 (29) (2014) 4920–4935.

[31] X. Li, J. Zhang, Y. Huo, K. Dai, S. Li, S. Chen, Two-dimensional sulfur- and chlorine-codoped g-C_3N_4/CdSe-amine heterostructures nanocomposite with effective interfacial charge transfer and mechanism insight, Appl. Catal., B 280 (2021) 119452.

[32] L. Liu, T. Hu, K. Dai, J. Zhang, C. Liang, A novel step-scheme $BiVO_4$/Ag_3VO_4 photocatalyst for enhanced photocatalytic degradation activity under visible light irradiation, Chin. J. Catal. 42 (1) (2021) 46–55.

[33] T. Hu, K. Dai, J. Zhang, S. Chen, Noble-metal-free Ni_2P modified step-scheme $SnNb_2O_6$/CdS-diethylenetriamine for photocatalytic hydrogen production under broadband light irradiation, Appl. Catal., B 269 (2020) 118844.

[34] F. Mei, Z. Li, K. Dai, J. Zhang, C. Liang, Step-scheme porous g-C_3N_4/$Zn_{0.2}Cd_{0.8}S$-DETA composites for efficient and stable photocatalytic H_2 production, Chin. J. Catal. 41 (1) (2020) 41–49.

[35] Y. Huo, J. Zhang, K. Dai, Q. Li, J. Lv, G. Zhu, C. Liang, All-solid-state artificial Z-scheme porous g-C_3N_4/Sn_2S_3-DETA heterostructure photocatalyst with enhanced performance in photocatalytic CO_2 reduction, Appl. Catal., B 241 (2019) 528–538.

[36] J. Li, X. Liu, L. Tan, Z. Cui, X. Yang, Y. Liang, Z. Li, S. Zhu, Y. Zheng, K.W.K. Yeung, X. Wang, S. Wu, Zinc-doped Prussian blue enhances photothermal clearance of *Staphylococcus aureus* and promotes tissue repair in infected wounds, Nat. Commun. 10 (1) (2019) 4490.

[37] X. Xie, C. Mao, X. Liu, L. Tan, Z. Cui, X. Yang, S. Zhu, Z. Li, X. Yuan, Y. Zheng, K.W. K. Yeung, P.K. Chu, S. Wu, Tuning the bandgap of photo-sensitive polydopamine/Ag_3PO_4/graphene oxide coating for rapid, noninvasive disinfection of implants, ACS Cent. Sci. 4 (6) (2018) 724–738.

[38] C. Mao, Y. Xiang, X. Liu, Z. Cui, X. Yang, Z. Li, S. Zhu, Y. Zheng, K.W.K. Yeung, S. Wu, Repeatable photodynamic therapy with triggered signaling pathways of fibroblast cell proliferation and differentiation to promote bacteria-accompanied wound healing, ACS Nano 12 (2) (2018) 1747–1759.

[39] S. Kim, T. Tachikawa, M. Fujitsuka, T. Majima, Far-red fluorescence probe for monitoring singlet oxygen during photodynamic therapy, J. Am. Chem. Soc. 136 (33) (2014) 11707–11715.

[40] P. Liang, X. Huang, Y. Wang, D. Chen, C. Ou, Q. Zhang, J. Shao, W. Huang, X. Dong, Tumor-microenvironment-responsive nanoconjugate for synergistic antivascular activity and phototherapy, ACS Nano 12 (11) (2018) 11446–11457.

[41] Y. Li, X. Liu, B. Li, Y. Zheng, Y. Han, D.F. Chen, K.W.K. Yeung, Z. Cui, Y. Liang, Z. Li, S. Zhu, X. Wang, S. Wu, Near-infrared light triggered phototherapy and immunotherapy for elimination of methicillin-resistant *Staphylococcus aureus* biofilm infection on bone implant, ACS Nano 14 (7) (2020) 8157–8170.

[42] X. Xie, C. Mao, X. Liu, Y. Zhang, Z. Cui, X. Yang, K.W.K. Yeung, H. Pan, P.K. Chu, S. Wu, Synergistic bacteria killing through photodynamic and physical actions of graphene oxide/Ag/collagen coating, ACS Appl. Mater. Interfaces 9 (31) (2017) 26417–26428.

[43] C. Mao, Y. Xiang, X. Liu, Z. Cui, X. Yang, K.W.K. Yeung, H. Pan, X. Wang, P.K. Chu, S. Wu, Photo-inspired antibacterial activity and wound healing acceleration by hydrogel embedded with Ag/Ag@AgCl/ZnO nanostructures, ACS Nano 11 (9) (2017) 9010–9021.

[44] M. Li, L. Li, K. Su, X. Liu, T. Zhang, Y. Liang, D. Jing, X. Yang, D. Zheng, Z. Cui, Z. Li, S. Zhu, K.W.K. Yeung, Y. Zheng, X. Wang, S. Wu, Highly effective and noninvasive near-infrared eradication of a *Staphylococcus aureus* biofilm on implants by a photoresponsive coating within 20 min, Adv. Sci. 6 (17) (2019) 1900599.

[45] Y. Luo, J. Li, X. Liu, L. Tan, Z. Cui, X. Feng, X. Yang, Y. Liang, Z. Li, S. Zhu, Y. Zheng, K.W.K. Yeung, C. Yang, X. Wang, S. Wu, Dual metal-organic framework heterointerface, ACS Cent. Sci. 5 (9) (2019) 1591–1601.

[46] Y. Li, X. Liu, L. Tan, Z. Cui, D. Jing, X. Yang, Y. Liang, Z. Li, S. Zhu, Y. Zheng, K.W. K. Yeung, D. Zheng, X. Wang, S. Wu, Eradicating multidrug-resistant bacteria rapidly using a multi functional g-C_3N_4@Bi_2S_3 nanorod heterojunction with or without antibiotics, Adv. Funct. Mater. 29 (20) (2019) 1900946.

[47] B. Huang, L. Tan, X. Liu, J. Li, S. Wu, A facile fabrication of novel stuff with antibacterial property and osteogenic promotion utilizing red phosphorus and near-infrared light, Bioact. Mater. 4 (1) (2019) 17–21.

[48] Y. Li, X. Liu, L. Tan, Z. Cui, X. Yang, Y. Zheng, K.W.K. Yeung, P.K. Chu, S. Wu, Rapid sterilization and accelerated wound healing using Zn^{2+} and graphene oxide modified g-C_3N_4 under dual light irradiation, Adv. Funct. Mater. 28 (30) (2018) 1800299.

[49] D. Han, Y. Han, J. Li, X. Liu, K.W.K. Yeung, Y. Zheng, Z. Cui, X. Yang, Y. Liang, Z. Li, S. Zhu, X. Yuan, X. Feng, C. Yang, S. Wu, Enhanced photocatalytic activity and photothermal effects of Cu-doped metal-organic frameworks for rapid treatment of bacteria-infected wounds, Appl. Catal., B 261 (2020) 118248.

[50] J. Jenkins, J. Mantell, C. Neal, A. Gholinia, P. Verkade, A.H. Nobbs, B. Su, Antibacterial effects of nanopillar surfaces are mediated by cell impedance, penetration and induction of oxidative stress, Nat. Commun. 11 (1) (2020) 1626.

[51] A. Tripathy, P. Sen, B. Su, W.H. Briscoe, Natural and bioinspired nanostructured bactericidal surfaces, Adv. Colloid Interface Sci. 248 (2017) 85–104.

[52] J. Li, L. Tan, X. Liu, Z. Cui, X. Yang, K.W.K. Yeung, P.K. Chu, S. Wu, Balancing bacteria-osteoblast competition through selective physical puncture and biofunctionalization of ZnO/polydopamine/arginine-glycine-aspartic acid-cysteine nanorods, ACS Nano 11 (11) (2017) 11250–11263.

[53] L. Liu, S. Chen, X. Zhang, Z. Xue, S. Cui, X. Hua, B. Yang, H. Yan, C. Liu, J. Wang, Z. Zhang, W. Yu, F. Wu, W. Xu, V.P. Lehto, T. Yue, Y. Liu, Y. Yu, T. Wang, J. Wang, Mechanical penetration of β-Lactam-resistant Gram-negative bacteria by programmable nanowires, Sci. Adv. 6 (27) (2020), eabb9593.

[54] E.P. Ivanova, J. Hasan, H.K. Webb, G. Gervinskas, S. Juodkazis, V.K. Truong, A.H. F. Wu, R.N. Lamb, V.A. Baulin, G.S. Watson, J.A. Watson, D.E. Mainwaring, R. J. Crawford, Bactericidal activity of black silicon, Nat. Commun. 4 (1) (2013) 2838.

[55] T. Wang, Z. Weng, X. Liu, K.W.K. Yeung, H. Pan, S. Wu, Controlled release and biocompatibility of polymer/titania nanotube array system on titanium implants, Bioact. Mater. 2 (1) (2017) 44–50.

[56] J. Shao, W. Sheng, M. Wang, S. Li, J. Chen, Y. Zhang, S. Cao, *In-situ* synthesis of carbon-doped TiO₂ single-crystal nanorods with a remarkably photocatalytic efficiency, Appl. Catal., B 209 (2017) 311–319.

[57] J. Li, D. Yi, F. Zhan, B. Zhou, D. Gao, D. Guo, S. Liu, X. Wang, J. Yao, Monolayered Ru-1/TiO₂ nanosheet enables efficient visible-light-driven hydrogen evolution, Appl. Catal., B 271 (2020) 118925.

[58] J. Wang, H.J. Chen, T. Hang, Y. Yu, G. Liu, G. He, S. Xiao, B.R. Yang, C. Yang, F. Liu, J. Tao, M.X. Wu, X. Xie, Physical activation of innate immunity by spiky particles, Nat. Nanotechnol. 13 (11) (2018) 1078–1086.

[59] X. Pan, Y.J. Xu, Defect-mediated growth of noble-metal (Ag, Pt, and Pd) nanoparticles on TiO₂ with oxygen vacancies for photocatalytic redox reactions under visible light, J. Phys. Chem. C 117 (35) (2013) 17996–18005.

[60] Q. Kang, J. Cao, Y. Zhang, L. Liu, H. Xu, J. Ye, Reduced TiO₂ nanotube arrays for photoelectrochemical water splitting, J. Mater. Chem. 1 (18) (2013) 5766–5774.

[61] X. Chen, L. Liu, F. Huang, Black titanium dioxide (TiO₂) nanomaterials, Chem. Soc. Rev. 44 (7) (2015) 1861–1885.

[62] H. Jiang, S.X. Sun, Morphology, growth, and size limit of bacterial cells, Phys. Rev. Lett. 105 (2) (2010), 028101.

[63] A.N. Malmi-Kakkada, D. Thirumalai, Generalized Rayleigh-Plesset theory for cell size maintenance in viruses and bacteria, BioRxiv (2019), https://doi.org/ 10.1101/552778.

[64] Y. Li, P. Wang, C. Huang, W. Yao, Q. Wu, Q. Xu, Synthesis and photocatalytic activity of ultrafine Ag₃PO₄ nanoparticles on oxygen vacated TiO₂, Appl. Catal., B 205 (2017) 489–497.

[65] X. Liu, Z. Xing, Y. Zhang, Z. Li, X. Wu, S. Tan, X. Yu, Q. Zhu, W. Zhou, Fabrication of 3D flower-like black N-TiO₂₋ₓ@MoS₂ for unprecedented-high visible-light-driven photocatalytic performance, Appl. Catal., B 201 (2017) 119–127.

[66] J. Qin, J. Huo, P. Zhang, J. Zeng, T. Wang, H. Zeng, Improving the photocatalytic hydrogen production of Ag/g-C₃N₄ nanocomposites by dye-sensitization under visible light irradiation, Nanoscale 8 (4) (2016) 2249–2259.

[67] A. Naldoni, M. Allieta, S. Santangelo, M. Marelli, F. Fabbri, S. Cappelli, C. L. Bianchi, R. Psaro, V. Dal Santo, Effect of nature and location of defects on bandgap narrowing in black TiO₂ nanoparticles, J. Am. Chem. Soc. 134 (18) (2012) 7600–7603.

[68] Y. Xu, H. Li, B. Sun, P. Qiao, L. Ren, G. Tian, B. Jiang, K. Pan, W. Zhou, Surface oxygen vacancy defect-promoted electron-hole separation for porous defective ZnO hexagonal plates and enhanced solar-driven photocatalytic performance, Chem. Eng. J. 379 (2020) 122295.

[69] X. Lu, G. Wang, T. Zhai, M. Yu, J. Gan, Y. Tong, Y. Li, Hydrogenated TiO₂ nanotube arrays for supercapacitors, Nano Lett. 12 (3) (2012) 1690–1696.

[70] Y. Guo, S. Chen, Y. Yu, H. Tian, Y. Zhao, J.C. Ren, C. Huang, H. Bian, M. Huang, L. An, Y. Li, R. Zhang, Hydrogen-location-sensitive modulation of the redox reactivity for oxygen-deficient TiO₂, J. Am. Chem. Soc. 141 (21) (2019) 8407–8411.

[71] E. McCafferty, J.P. Wightman, Determination of the concentration of surface hydroxyl groups on metal oxide films by a quantitative XPS method, Surf. Interface Anal. 26 (8) (1998) 549–564.

[72] N.O. Gopal, H.H. Lo, T.F. Ke, C.H. Lee, C.C. Chou, J.D. Wu, S.C. Sheu, S.C. Ke, Visible light active phosphorus-doped TiO₂ nanoparticles: an EPR evidence for the enhanced charge separation, J. Phys. Chem. C 116 (30) (2012) 16191–16197.

[73] Y. Liu, L. Fang, H. Lu, Y. Li, C. Hu, H. Yu, One-pot pyridine-assisted synthesis of visible-light-driven photocatalyst Ag/Ag₃PO₄, Appl. Catal., B 115 (2012) 245–252.

[74] H. Zhang, G. Wang, D. Chen, X. Lv, J. Li, Tuning photoelectrochemical performances of Ag-TiO₂ nanocomposites via reduction/oxidation of Ag, Chem. Mater. 20 (20) (2008) 6543–6549.

[75] M. Zhu, P. Chen, M. Liu, Graphene oxide enwrapped Ag/AgX (X = Br, Cl) nanocomposite as a highly efficient visible-light plasmonic photocatalyst, ACS Nano 5 (6) (2011) 4529–4536.

[76] W. Fan, H. Li, F. Zhao, X. Xiao, Y. Huang, H. Ji, Y. Tong, Boosting the photocatalytic performance of (001) bioi: enhancing donor density and separation efficiency of photogenerated electrons and holes, Chem. Commun. 52 (30) (2016) 5316–5319.

[77] S. Li, J. Qiu, M. Ling, F. Peng, B. Wood, S. Zhang, Photoelectrochemical characterization of hydrogenated TiO₂ nanotubes as photoanodes for sensing applications, ACS Appl. Mater. Interfaces 5 (21) (2013) 11129–11135.

[78] M. Michelswirth, M. Räkers, C. Schäfer, J. Mattay, M. Neumann, U. Heinzmann, Photocycloaddition of anthracene-functionalized monolayers on silicon (100) surface, J. Phys. Chem. B 114 (10) (2010) 3482–3487.

[79] Y. Li, X. Xu, Y. Li, C. Ding, J. Wu, A. Lu, H. Ding, S. Qin, C. Wang, Absolute band structure determination on naturally occurring rutile with complex chemistry: implications for mineral photocatalysis on both earth and mars, Appl. Surf. Sci. 439 (2018) 660–671.

[80] C. Tang, E. Liu, J. Wan, X. Hu, J. Fan, Co₃O₄ nanoparticles decorated Ag₃PO₄ tetrapods as an efficient visible-light-driven heterojunction photocatalyst, Appl. Catal., B 181 (2016) 707–715.

[81] H. Ding, H. Han, Y. Han, Y. Liang, X. Liu, Z. Li, S. Zhu, S. Wu, Visible light responsive CuS/protonated g-C₃N₄ heterostructure for rapid sterilization, J. Hazard Mater. 393 (2020) 122423.

[82] P. Kuppusamy, J.L. Zweier, Characterization of free radical generation by xanthine-oxidase: evidence for hydroxyl radical generation, J. Biol. Chem. 264 (17) (1989) 9880–9884.

[83] E. Evans, V. Heinrich, F. Ludwig, W. Rawicz, Dynamic tension spectroscopy and strength of biomembranes, Biophys. J. 85 (4) (2003) 2342–2350.

[84] X. Xie, A.M. Xu, M.R. Angle, N. Tayebi, P. Verma, N.A. Melosh, Mechanical model of vertical nanowire cell penetration, Nano Lett. 13 (12) (2013) 6002–6008.

[85] A. Panacek, L. Kvitek, M. Smekalova, R. Vecerova, M. Kolar, M. Roderova, F. Dycka, M. Sebela, R. Prucek, O. Tomanec, R. Zboril, Bacterial resistance to silver nanoparticles and how to overcome it, Nat. Nanotechnol. 13 (1) (2018) 65–71.

[86] Y. Lai, L. Dong, H. Zhou, B. Yan, Y. Chen, Y. Cai, J. Liu, Coexposed nanoparticulate Ag alleviates the acute toxicity induced by ionic Ag⁺ in vivo, Sci. Total Environ. 723 (2020) 138050.